Origin of antiferroelectricity in NaNbO₃

Niloofar Hadaeghi ⬤, Mian Dai, Yixuan Zhang, Ruiwen Xie, Hamid Nouri, and Hongbin Zhang ⬤[*]

Institute of Materials Science, Technical University of Darmstadt, Otto-Berndt-Straße 3, Darmstadt 64287, Germany

The stabilization and origin of antiferroelectricity in the antiferroelectric (AFE) materials have always been the tools to facilitate the AFE/FE engineering. However, the mechanistic understanding of the driving forces, especially in the electronic level, is still elusive. Here, combining density functional theory calculations and symmetry analysis, following the pseudo-Jahn-Teller effect (PJTE) theory, we investigate both the stabilization and origin of antiferroelectricity in the AFE perovskite NaNbO₃. Utilizing the potential energy surface and effective Hamiltonian, it is observed that the cooperative couplings play a critical role to stabilize the AFE phase. Moreover, considering adiabatic potential energy surface cross sections at Γ on the basis of the PJTE, the origin of the cubic-AFE phase transition at Γ is observed as the coupling of (T_{2u}, T_{2g}) electronic states, inducing the Δ_5 mode, whereas both the (T_{1u}, T_{2g}) state and (T_{2u}, T_{2g}) state couplings via the Γ_4^- mode are the reason behind the cubic to ferroelectric phase transition at Γ.

I. INTRODUCTION

Ferroelectric (FE) and antiferroelectric (AFE) materials are two classes of polarizable materials which have attracted intensive attention due to their vast spectrum of applications in the nonvolatile random access memories [1–3] and high energy capacitors [4–6]. To develop mechanistic understanding of the functionalities of these materials and further to design materials with optimal performance, it is indispensable to elucidate how the finite order parameters couple with the structural phase transitions, where the knowledge about the underlying driving forces at the electronic level is still limited. In the FE materials, it is known that a delicate interplay exists between the long-range dipole-dipole interaction which favors the FE ordering and the short-range repulsion which is in favor of the cubic phase [7–10]. The short-range interaction weakening, particularly in BaTiO₃, PbTiO₃, and KNbO₃ as the examples, is attributed to a soft lattice mode at the Γ point. That leads to the *B*-site cation displacement, described by the FE Γ_4^- distortion mode. Such distortions along with the strain modes then stabilize the FE phase [11,12]. The origin of the short-range interaction weakening is attributed to the pseudo-Jahn-Teller effect (PJTE) [10,13]. The effect originates the structural phase transformations by the coupling of the nuclei displacements with the mixing of the ground and excited electronic states [14–17]. For instance, the origin of forming the FE structure in BaTiO₃ is proved to be mixing of the T_{2g} excited state with the T_{1u} or T_{2u} valance states, which provides the local instability by inducing the Γ_4^- distortion mode [10].

The interplay between the short-range and long-range interactions is prevalent also in AFE materials [18–25], leading to intriguing structural phase transitions [26] described by different soft lattice modes. For instance, the phase transition in PbZrO₃ is described by a combination of three dominant distortion modes, corresponding to the Σ, R [26,27], and S points [27]. The potential energy curve together with the invariant polynomial show the cooperation of the mutual interactions of the modes, as well as their trilinear coupling, to stabilize the AFE phase of the compound [26,27]. Besides, the origin of antiferroelectricity in the material is attributed to a single polar mode, via flexoelectric coupling [26]. However, the electronic driving force of forming such structure, not only in PbZrO₃ but also in many other AFE materials, is not yet clear. On the other hand, the origin in AFE H₂C₄O₄ is elucidated to be due to the electron-phonon interaction, as the PJTE [28]. In SbSI and SbSeI, the electronic reason behind the electric field induced AFE-FE phase transition is studied to be the PJTE as well, inducing the Sb atom displacement from its equilibrium positions [29].

NaNbO₃ is an AFE material at room temperature, which has always been interesting since its discovery due to its electric field induced AFE-FE phase transition and the increasing environmental concerns on the Pb-based materials [30–34]. The compound crystallizes in the cubic paraelectric (PE) structure at about 900 K and contains several soft lattice modes which lead to a complex sequence of phase transitions, as shown in Fig. 1 [35–41]. The structure of the *P* phase with the *Pbcm* space group contains the AFE Na2 and Nb ion displacements along the [010] direction and combination of the $a^- a^- b^+$ and $a^- a^- b^-$ tilting of oxygen octahedra based on the Glazor notation [36,42,43]. Assuming the cell of this phase as two subcells with the $c/2$ length, the distortions in the subcells are in the opposite manner with respect to each other, which leads to the antiferroelectricity [43]. Under application of the critical electric field, the distortions in the two subcells behave in the same manner and the AFE phase transforms to a FE structure with the half dimension [43]. The electric field induced FE phase is known as the metastable *Q* phase which crystallizes in the orthorhombic $Pmc2_1$ structure [44,45] and coexists with the AFE *P* phase [31–34,46]. It contains the
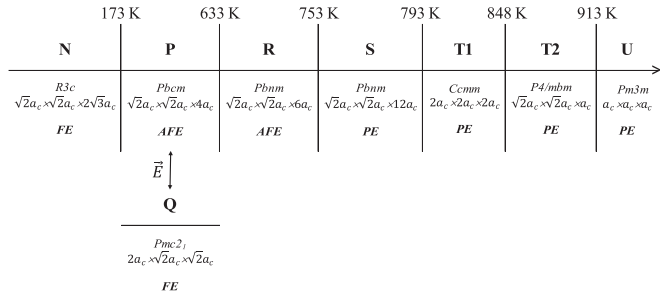

FIG. 1. Phase transition consequence through decreasing temperature. The Q phase is the electric field induced FE phase, coexisting with the AFE P phase.

parallel Nb displacement along its [001] direction, as well as the tilting of the oxygen octahedra, described as $a^+b^-b^-$ [32,47,48]. The structures of the AFE and FE phases along with the cubic phase are shown in Fig. 2. The stabilization of the AFE phase has been previously studied to be due to the tiltings of octahedra [49]; however, the reason behind antiferroelectricity and what differences exist compared to the FE phase in the electronic level is still an elusive point.

In this work, we perform density functional theory (DFT) calculations and detailed symmetry analysis following the concept of the PJTE [16,50] to investigate the origin of the direct cubic to AFE phase transition in NaNbO$_3$. To our aim, the distortions in the AFE and FE phases are decomposed based on the symmetric distortion modes and the most primary ones are considered for further analysis. The invariant polynomial, expanded up to the fourth order terms, together with the potential energy curve are investigated to follow the primary mode interactions in the AFE phase stabilization. Based on the obtained polynomial coefficients, the trilinear coupling and also the coupling of the AFE mode with the modes responsible for the tilting of oxygen octahedra, as well as the strain modes, are indispensable to stabilize the AFE phase. Furthermore, focusing on the second order terms of the energy expansion in terms of the PJTE together with the symmetry arguments and

the evaluation of the cross sections of the adiabatic potential energy surface (APES), we find the electronic origin of the phase transitions at Γ. That, in the PE-AFE phase transition, is the (T_{2u}, T_{2g}) electronic states coupling via the AFE Δ_5 mode, whereas the PE-FE phase transition is driven by coupling of both the (T_{1u}, T_{2g}) states and the (T_{2u}, T_{2g}) states, inducing the Γ_4^- mode. Therefore, the T_{1u} state would be able to determine which phase transition to take place.

II. COMPUTATIONAL DETAILS

The energy landscape calculations were performed using the projector augmented wave (PAW) method [52] as implemented in the Vienna *Ab initio* Simulation Package (VASP) [53,54]. The experimental structures of the PE, AFE, and FE phases [48,55] were fully optimized for both the lattice parameters and atom positions with forces converged to be less than 5×10^{-4} eV/Å. The cutoff energy for the plane wave basis for both the structural relaxation and total energy evaluation was set to be 550 eV.

For the PJTE part, to further analyze the electronic structure, we utilized the full potential augmented plane waves plus local orbitals [FP-(L)APW+lo] method [56,57] as implemented in WIEN2k code [58] and also the full-potential local-orbital minimum-basis (FPLO) package [59,60]. The irreducible representations (irreps) of the bands in the high-symmetry structures were calculated using the WIEN2k package. The values of R_{MT} for Na, Nb, and O ions were considered as 2.5, 1.96, and 1.77 a.u., respectively. The $R_{MT}K_{max}$ was optimized to be 8. Inside the MT spheres the maximum value of angular momentum $l_{max} = 10$ was used. The charge density and potential were Fourier expanded up to $G_{MAX} = 14\sqrt{Ry}$ in the interstitial region. To evaluate the cross sections of the APES, band structure unfolding as implemented in the FPLO code, was performed.

To have the consistency, for all calculations the exchange-correlation functional was approximated using the generalized gradient approximation (GGA) as parametrized by Perdew-Burke-Ernzerhof (PBE) [61] and the effective k mesh [62] was utilized as $13 \times 13 \times 13$ for the cubic, $9 \times 9 \times 3$ for the AFE, and $6 \times 9 \times 9$ for the FE phases in the supercell geometry to ensure the good convergence. Besides, as we used three codes, to ensure the consistency, the band structures using three codes were compared, and the results were the same.

III. RESULTS AND DISCUSSION

To figure out the origin of antiferroelectricity in NaNbO$_3$, the distortion modes driving the phase transitions from the PE $Pm\bar{3}m$ phase to the AFE $Pbcm$ phase, and from the PE phase to the electric-field induced FE $Pmc2_1$ phase, are identified using ISODISTORT [63], as listed in Table I. Obviously, the R_5^-, T_2, and Δ_5 distortion modes are the primary symmetry modes causing the phase transition from the cubic to the AFE phase, and the R_5^-, Γ_4^-, and M_2^+ distortion modes are the primary ones for the cubic to FE phase transition, where the corresponding displacement patterns of atoms for each mode are shown in Fig. 3. In the cubic to AFE phase transition, the Δ_5 mode modulates according to the wave vector $q_\Delta = 2\pi(0, 1/4, 0)/a$ of the five-atom cubic structure. It involves the displacements
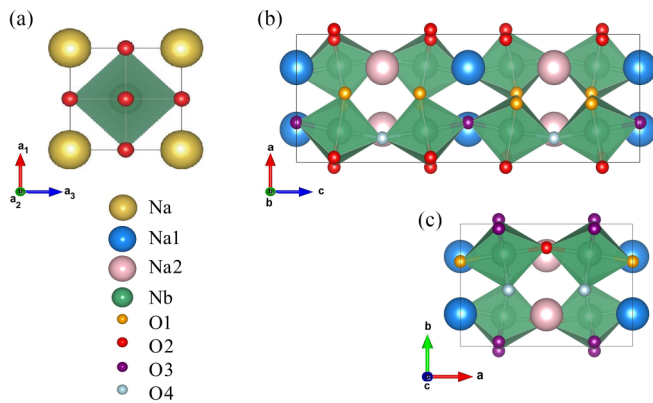

FIG. 2. Structures of (a) cubic phase with 5 atoms, (b) AFE phase with 40 atoms, and (c) FE phase with 20 atoms, using VESTA [51]. If we define the $a_1 = (1, 0, 0)$, $a_2 = (0, 1, 0)$, and $a_3 = (0, 0, 1)$ vectors for the cubic cell in Cartesian reference, the vectors for the AFE phase are given as $a = a_1 - a_2$, $b = a_1 + a_2$, and $c = 4a_3$, and those for the FE one are defined as $a = 2a_1$, $b = a_2 - a_3$, and $c = a_2 + a_3$.

TABLE I. The distortion modes corresponding to the phase transition from the cubic PE structure to the AFE (*Pbcm*) and FE (*Pmc*2_1) phases. The symmetry labels are defined for the setting when the *B*-site cation is positioned on the origin. For the amplitudes, we use parent normalized amplitudes (A_p), to make the comparison of the amplitude of the different distortion modes possible.

		Distortion and amplitudes (A_p) (Å)		
AFE	Displacive modes	$R_5^-(0.49527)$	$T_2(0.42239)$	$\Delta_5(0.25681)$
		$M_5^-(0.04711)$	$T_4(0.01278)$	$X_1^+(0.00529)$
	Strain modes	$\Gamma_1^+(-0.01483)$	$\Gamma_3^+(-0.01330)$	$\Gamma_5^+(0.00959)$
FE	Displacive modes	$R_5^-(0.90625)$	$\Gamma_4^-(0.85566)$	$M_2^+(0.83187)$
		$M_5^-(0.15335)$	$X_5^-(0.14952)$	$\Gamma_5^-(0.07044)$
	Strain modes	$\Gamma_3^+(-0.01493)$	$\Gamma_1^+(-0.01105)$	$\Gamma_5^+(0.00800)$

of Nb and Na2 cations along the pseudocubic [010] direction with the AFE nature, while Na1 ions are fixed. This mode also contains the negligibly small relative displacements of the O1 and O2 ions with respect to the Nb ion displacements in the (001) plane, where the displacements along the *b* axis are much larger than those along the *a* axis. In this mode the O3 ions are fixed, while O4 ions are displaced along the [010] direction with the AFE nature. The zone boundary antiferrodistortive (AFD) R_5^- mode, associated with the wave vector $q_R = 2\pi(1/2, 1/2, 1/2)/a$, involves the in-phase rotations of all O ions around the *b* axis. The adjacent octahedrons show the opposite rotation orientations along the [1$\bar{1}$0] direction and along the *c* axis. In the mode, all the other atoms are at fixed positions. The T_2 mode, with the $q_T = 2\pi(1/2, 1/2, 1/4)/a$ wave vector, contains combination of the in-phase and out-of-phase rotations of the O1 and O2 ions about the *c* axis in the (001) plane.

FIG. 3. The primary distortion modes for the cubic to the AFE and to the electric field induced FE phase transitions in NaNbO₃. (a) The displacement of the Na2 and Nb ions by Δ_5 mode, (b) the AFD R_5^- mode, and (c) the AFD T_2 mode, for the cubic to AFE phase transition. (d) The FE displacement of Nb ions by the Γ_4^- mode, (e) the AFD R_5^- mode, and (f) the AFD M_2^+ mode, for the cubic to FE phase transition.

In the case of the cubic to electric field induced FE phase transition, the Γ_4^- mode, modulated based on $q_\Gamma = 2\pi(0, 0, 0)/a$, is responsible for the FE displacement of the Nb ions along the [001] direction, where the O1 and O2 ions displace along the [001] direction and the O3 and O4 ions are displaced in the (100) plane. However, as the displacements of the O3 and O4 ions along the [001] direction are much larger than that along the [010] one, it can be considered that all O ions have relative displacements with respect to the Nb ion displacements along the *c* axis. The AFD R_5^- mode is modulated as $q_R = 2\pi(1/2, 1/2, 1/2)/a$ and contains the rotations of all O ions around the *c* axis. Two adjacent octahedrons have opposite rotation orientation along the [011] and [100] directions. The M_2^+ mode, which is modulated as $q_M = 2\pi(1/2, 1/2, 0)/a$, contributes to the in-phase rotation of the O3 and O4 ions around the *a* axis, while the rotations have opposite orientations along [011] axis. All the other atoms are fixed for this mode.
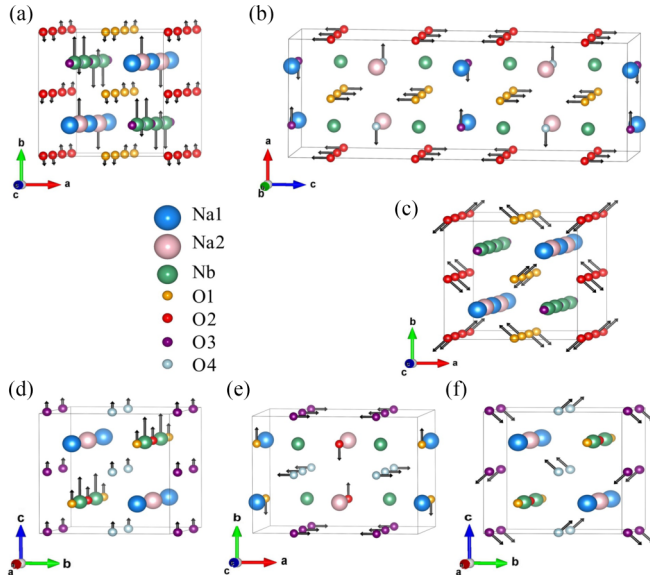
A. Energy landscape

Without an intention to evaluate the energy landscape of all the possible phase transitions in NaNbO₃ and with focusing on the direct cubic-AFE phase transition, we describe the energy of the AFE phase by a polynomial. In that, following the Landau theory of the phase transitions, each term is invariant under the high-symmetry group by using the symmetry-allowed invariants and coupling polynomials [64,65]. The invariant polynomial of the normalized primary distortion mode amplitudes, using the INVARIANTS code [66], where the *Q* values are unitless parameters and the normalization is done to one with respect to the fully relaxed AFE phase (meaning that, for instance, $Q_\Delta = 1$ describes the Δ_5 mode amplitude value in the fully relaxed AFE structure), is

$$
\begin{aligned}
E = E_{\text{cubic}} &+ A_\Delta Q_\Delta^2 + B_\Delta Q_\Delta^4 + A_R Q_R^2 + B_R Q_R^4 \\
&+ A_T Q_T^2 + B_T Q_T^4 + D_{\Delta R} Q_\Delta^2 Q_R^2 + D_{\Delta T} Q_\Delta^2 Q_T^2 \\
&+ D_{TR} Q_T^2 Q_R^2 + C_{\Delta RT} Q_\Delta Q_T Q_R.
\end{aligned} \tag{1}
$$

Figure 4 shows the energy landscape along different paths in the phase space spanned by the three primary modes [27]. By fitting the DFT calculated energies in Fig. 4 on to Eq. (1), we find the values of the coefficients, which all are important to investigate how different distortion
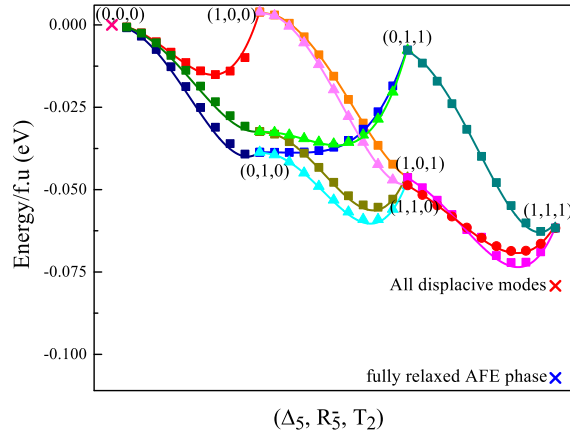
FIG. 4. The potential energy curve considering the primary distortion modes, where the scatter points are the DFT calculated energies and the curves are the fitted curves using the polynomial. The numbers in parentheses show the value of the amplitudes, where they are normalized to 1; e.g., 1 and 0 in the terms such as (1,0,0) represent the amplitude of the corresponding mode to be the same as that in the fully relaxed AFE structure and 0, respectively. (0,0,0) structure is the $\sqrt{2} \times \sqrt{2} \times 4$ supercell of the cubic phase. The strain modes in all structures (except the structure of fully relaxed AFE phase) are considered to be zero.

modes interact to stabilize the AFE phase. The coefficients are achieved as (with eV/f.u. units) $A_\Delta = -0.0645$, $B_\Delta = 0.0687$, $A_R = -0.0949$, $B_R = 0.0564$, $A_T = -0.0686$, $B_T = 0.0363$, $D_{\Delta R} = -0.0140$, $D_{\Delta T} = -0.0170$, $D_{TR} = 0.0631$, $C_{\Delta RT} = -0.0250$.

Based on Fig. 4 and the values of the coefficients, it is observed that the R_5^- and T_2 modes gain more energy, compared to the Δ_5 mode, when they are applied individually. In the biquadratic couplings, $D_{\Delta R}$ and $D_{\Delta T}$ are both negative, while D_{TR} is positive. This indicates that the cooperation of the (Δ_5, R_5^-) and (Δ_5, T_2) pairs is in favor of stabilizing the AFE phase, while the (R_5^-, T_2) pair is not. The coexistence of displacive and AFD instabilities has already been shown to be very common in perovskites as well [67]. Besides, these results agree with the important role of the tilting of octahedra in the stabilization of the AFE phase in NaNbO$_3$ as already proved as well [49]. In order to study better how the modes are coupled together we study the situation shown in Fig. 5, where we study the energy of the system as a function of amplitude of one mode at different steps, in each of which the fixed value of the amplitude of another mode is considered and the later value changes for different steps. Based on Fig. 5(a), it is obvious that with increasing the amplitude of the Δ_5 mode, the system gains the minimum of energy at higher values of the R_5^- mode and it yields the cooperative coexistence of the (Δ_5, R_5^-) modes in the system, while upon enhancing the R_5^- mode, as shown in Fig. 5(b), the energy equilibrium position shifts to a lower value of the T_2 mode, which confirms that the (R_5^-, T_2) modes tend not to coexist in the absence of the Δ_5 mode, or in other words, that their coexistence does not favor the AFE phase stabilization. Studying the energy minimum position of the Δ_5 and R_5^- modes for three values of the T_2 mode amplitude leads to a similar conclusion as well. As shown in Figs. 5(c) and 5(d), the (T_2, Δ_5) modes can
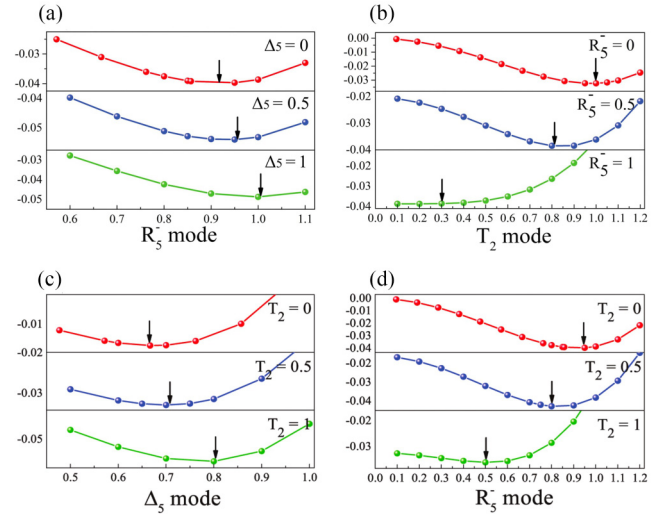

FIG. 5. The energy of the system as a function of (a) the R_5^- mode at different values of the Δ_5 mode, (b) the T_2 mode at different values of the R_5^- mode, and (c) and (d) the Δ_5 and R_5^- modes at different values of T_2 mode, respectively.

cooperatively coexist, while the (T_2, R_5^-) modes' coexistence, if the Δ_5 mode is absent, is not in favor of the AFE phase stabilization. The observed cooperative coupling between the AFE and AFD modes is in agreement with what is already seen for a wide range of temperatures and the electric field application in PbZrO$_3$ [26,68], SrTiO$_3$, YMnO$_3$, and LaAlO$_3$ for the large value of tiltings [69–71]. For instance in PbZrO$_3$, the coexistence of the Σ_2 and R_4^+ modes decreases the energy toward the AFE phase considerably, where the Σ_2 mode, corresponding to the AFE displacements of the Pb and Zr ions and marginal octahedral tiltings, dominantly has the AFE nature and the R_4^+ mode has the AFD nature. However, the bi-couplings between the (R_4^+, S_4) modes and (Σ_2, S_4) modes, where the S_4 mode has a low amplitude and mixed AFE and AFD nature, do not give rise to a significant change of the energy [27].

Based on Fig. 4 and also the value of $C_{\Delta RT}$, the gain of the energy by the trilinear term, i.e., when all three modes coexist, is considerable. That denotes the crucial role of this term, as without such a coupling the AFE phase could not be stabilized. This considerable gain of energy exists for any of the paths. Such an importance for the trilinear term exists for the PbZrO$_3$ AFE phase stabilization as well [27]. These three modes $(\Delta_5, R_5^-,$ and $T_2)$ [the situation (1,1,1)] decrease the energy of the cubic phase 64.31 (meV/f.u.), while the energy of the fully relaxed AFE structure is 107.15 (meV/f.u.) less than cubic phase. Thus, more than half (60.02%) of the energy gain is done by the three dominant displacive modes. The energy difference between the structure containing all displacive modes and the cubic phase is 79.22 (meV/f.u.). Therefore, all displacive modes provide 73.93% of the whole energy gain and the rest is provided by the strain modes (26.07%), which is a considerable value, while this value in PbZrO$_3$ is small [27].

Figure 6 shows the same procedure as done in Fig. 4, with considering the strain modes as well; where the strain modes
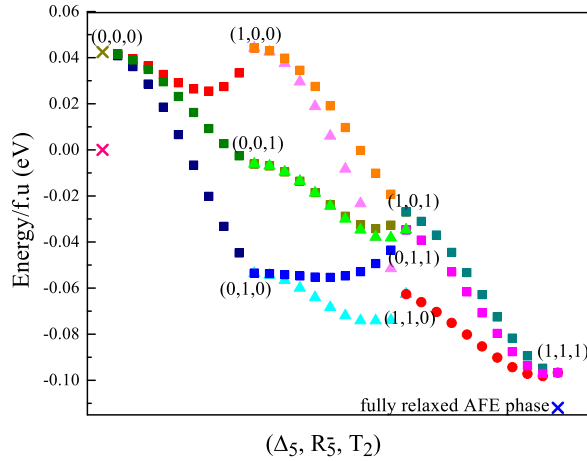
FIG. 6. The potential energy curve (obtained from DFT calculated energies), considering the strain modes as well. The numbers in parentheses have the same meaning as in Fig. 4, while the strain modes are present here. The pink cross represents the energy of the (0,0,0) structure in the absence of the strain modes.

for all structures are the same as in the fully relaxed AFE structure. Based on Fig. 6, the behavior of the individually applied modes does not change compared to when the strain modes are absent, whereas, in the presence of strain modes, the coexistence of the R_5^- and T_2 modes is cooperative. Just considering large values of the T_2 mode for the amplitude of $R_5^- = 1$, in the absence of the Δ_5 mode, increases the energy slightly. The strain modes are compressive along the (0,0,1) pseudocubic direction, and this decrease in lattice parameter helps the oxygen tilting modes to appear and coexist [69]. In the case of the trilinear term, its significant role is also observable when the strain modes are present.

In addition to the cubic-AFE energy landscape, the information about the AFE-FE phase transition and the FE phase stabilization is crucial in a deeper understanding. Therefore, some calculations and discussion regarding the symmetry and energy landscape analysis in the AFE-FE and cubic-FE phase transitions, respectively, are done and found in the Supplemental Material [72].

B. Pseudo-Jahn-Teller effect

To shed light on the electronic origin of phase transitions, or in other words the electronic driving force of the cubic phase destabilization in the cubic-AFE and cubic-FE phase transitions, we performed a detailed analysis following the PJTE, as previously introduced as the origin of ferroelectricity in the BaTiO₃ [10] case as well. Although to quantitatively decipher the electronic origin of the whole potential energy surface covering all couplings in the effective Hamiltonian, high-ordered electron-phonon interactions are required, to our aim focus on the Q^2 terms is enough. That is based on the PJTE theory, where the curvature of the potential energy surface gives us the clue about the destabilization of the high symmetry crystal structure, and can be quantified by focusing on the second order terms of the APES expansion [10,73]. Following the standard perturbation theory [73], the curvature of the APES of the ground state with respect to the high
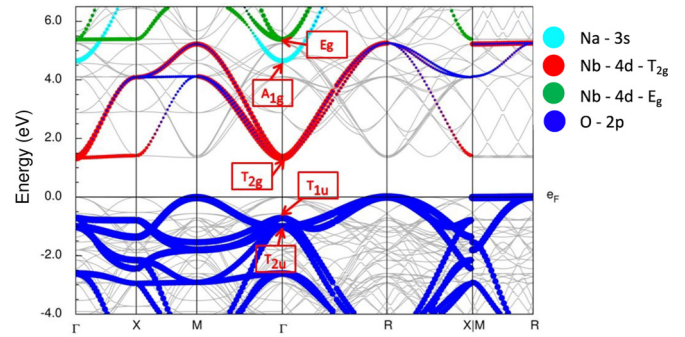

FIG. 7. Unfolded band structure of the supercell of the cubic phase along with symmetry of the states. The gray bands are the supercell (not-unfolded) band structures.

symmetry structure, i.e., $K = (\partial^2 E / \partial Q^2)_0$, consists of two terms [16], as

$$K = \underbrace{\left\langle \Psi_0 \left| \left(\frac{\partial^2 H}{\partial Q^2} \right)_0 \right| \Psi_0 \right\rangle}_{K_0} - \underbrace{2 \sum_n \frac{\left| \langle \Psi_0 | \left(\frac{\partial H}{\partial Q} \right)_0 | \Psi_n \rangle \right|^2}{E_n - E_0}}_{K_V}, \quad (2)$$

where H shows the Hamiltonian and Ψ_0 and Ψ_n represent the ground state and excited state wave functions, respectively. $E_n - E_0$ denotes the energy difference between the ground and excited states. If the high symmetry structure is unstable with respect to the Q distortion, the curvature of the APES of the ground state in the direction of the Q distortion is negative. The value of K_0 is proved to be positive in the high symmetry structure by many studies [74–76], whereas the K_V is negative and is identified as the main reason of instability, driving the phase transition [77–80]. The numerator of the K_V term in Eq. (2) contains the off-diagonal vibronic coupling constants, i.e., $F_{0n} = \langle \Psi_0 | (\frac{\partial H}{\partial Q})_0 | \Psi_n \rangle$, indicating how the ground and excited states are coupled via the vibrational mode Q. Thus, it actually studies the interatomic overlap of the wave functions by mixing of the ground and excited states [16]. The allowed transitions are achieved based on the symmetry analysis. The symmetry consideration is defined as $\Gamma_0 \otimes \Gamma_Q \otimes \Gamma_n \supset A_{1g}$; i.e., the direct product of the irreps of the ground state Γ_0, the excited state Γ_n, and the phonon mode Γ_Q must contain the totally symmetric representation A_{1g}. It can be rephrased as $\Gamma_0 \otimes \Gamma_n \supset \Gamma_Q$; i.e., the direct product of the irreps of the electronic states contains the irrep of the distortion mode [81]. Satisfying such condition provides the possibility of contribution to the K_V term.

In addition, the K_V term dominates the positive nonvibronic contribution (i.e., $K < 0$), if the PJTE is strong enough. The strong PJTE can be manifested by the adiabatic potential energy surface cross sections (APESCSs). APESCSs investigate whether any possible coupling of the ground and excited states is induced by a given symmetry-allowed distortion mode. In such scenario, the ground state in the APESCSs becomes unstable (with a negative curvature), and the excited state becomes stable (having positive curvature). In the current work, we consider the APESCSs for the Γ point of the Brillouin zone (BZ).
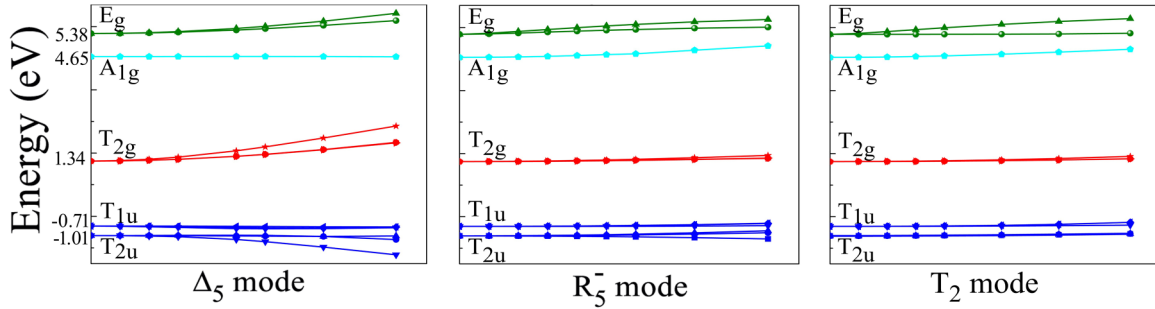
FIG. 8. APESCSs at Γ along the primary distortion modes. The structures are considered with the normalized amplitude of the given mode, changing from 0 to 1.

Figure 7 displays the unfolded band structure of the supercell of the high-symmetry cubic phase on the 5-atom structure, along with the irreps of the electronic states around the Fermi energy highlighted at Γ. The valence bands comprise mostly the O-$2p$ states of the T_{1u} and T_{2g} character, whereas the conduction bands are originated from the Nb-$4d$ states of both T_{2g} and E_g symmetry, and additionally the Na-$3s$ states with the totally symmetric irrep, i.e., A_{1g}.

For the APESCSs at Γ, the band structures with the given frozen-in distortion modes of increasing amplitudes are unfolded into the BZ of the 5-atom cubic structure, and the energies of different states at Γ are followed. The reference of energy is considered as the O-$1s$ state [82]. The approach has already been utilized in both 2-D and 3-D materials [83,84].

Using the ISODISTORT package [63], the Δ_5 primary mode is the composition of four irreps, as $T_{1u} + A_{2u} + E_{u1} + E_{u2}$, while the R_5^- and T_2 modes show the E_u irrep. Considering the symmetry analysis, it is straightforward to obtain

$$T_{2u} \otimes T_{2g} = A_{1u} + E_u + T_{1u} + T_{2u}, \qquad (3)$$

$$T_{2u} \otimes E_g = T_{1u} + T_{2u}, \qquad (4)$$

$$T_{1u} \otimes T_{2g} = A_{2u} + E_u + T_{1u} + T_{2u}, \qquad (5)$$

$$T_{1u} \otimes A_{1g} = T_{1u}, \qquad (6)$$

and

$$T_{1u} \otimes E_g = T_{1u} + T_{2u}. \qquad (7)$$

That is, the couplings of (T_{2u}, T_{2g}) and (T_{1u}, T_{2g}) electronic states are possible by Δ_5, R_5^-, or T_2 distortion modes, whereas the coupling of (T_{2u}, E_g), (T_{1u}, A_{1g}), and (T_{1u}, E_g) states could occur only via the Δ_5 distortion mode.

1. Cubic-AFE phase transition

The APESCSs at Γ are shown in Fig. 8 for the Δ_5, R_5^-, and T_2 distortion modes. It is observed that along the Δ_5 distortion mode, the energy of the T_{2u} state decreases and the energy of the T_{2g} and E_g states increases. This is considered as the destabilization of the T_{2u} state (as the ground state) and the stabilization of the T_{2g} and E_g states (as the excited states). In other words, the coupling between the (T_{2u}, T_{2g}) states and (T_{2u}, E_g) states induces the Δ_5 mode. The condition, showing the strong PJTE qualitatively, is considered as the electronic driving reason for the phase transition at Γ. Based on the

energy gap between the (T_{2u}, T_{2g}) states and between the (T_{2u}, E_g) states, and the K_V term in Eq. (2), the coupling between the (T_{2u}, T_{2g}) states is expected to be larger than that between the (T_{2u}, E_g) states. In the case of the R_5^- distortion mode, not only the destabilization of the T_{2u} state is much less than that along the Δ_5 mode, but also no stabilization of the excited states occurs; and in the case of the T_2 distortion mode, there is no destabilization for the T_{2u} state. Thus, there is no strong PJTE via R_5^- and T_2 distortion modes; i.e., they are not the source of instability at Γ. However, as seen in Eq. (1), the A_R and A_T, as the curvature of the APESCS in the R_5^- and T_2 directions, respectively, are negative. Therefore, they contribute to the instability of the cubic phase, but their electronic origins are at the other points of the BZ. Thus, it is interesting to evaluate APESCSs in the whole BZ so that the strong PJTE can be quantified more accurately, which will be saved for future studies. Previously, in the temperature dependent phase transitions of NaNbO$_3$ as shown in Fig. 1, the phase transition from the cubic to $T2$, $T1$, and S phases was attributed to the oxygen tiltings, while for the phase transition from P to N the polar mode plays a role [43,85,86], which is in agreement with the important role of the Δ_5 mode to drive the direct cubic-AFE phase transition in our calculation. Moreover, it is concluded that the strong PJTE at Γ could be more important than the other points in the AFE phase transition. That is also similar to the PbZrO$_3$ case as well, where both AFE and octahedral tilting distortions are the primary order parameters, while the latter is claimed to occur at higher temperature range through decreasing the temperature from the cubic phase [68,87].

The APESCSs (Fig. 8) results, along with the information about the different biquadratic couplings in either the presence or the absence of the strain modes, lead into the conclusion that the Δ_5 mode has an essential contribution in the destabilization of the cubic phase and starting the phase transition based on PJTE, and the R_5^- and T_2 modes along with strain modes mostly contribute to the AFE phase stabilization, by decreasing the energy. The situation is similar to PbZrO$_3$ case. In that case, the mode at the Σ point, containing the AFE distortion, as the original mode, induces the octahedral tiltings at the R point by the biquadratic couplings [26], while the octahedral tiltings are further necessary to stabilize the AFE phase [27].

We further studied the APESCSs at Γ for the submodes of the Δ_5 mode to figure out the main distortion responsible for cubic structure instability. As the amplitudes of A_{2u} and E_{u1} are very small, we study only the APESCSs related to
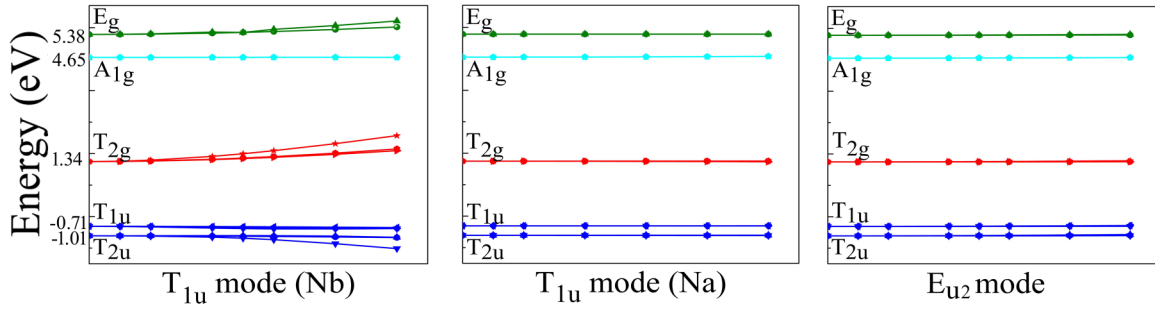
FIG. 9. APESCSs at Γ along the submodes of the Δ_5 mode. T_{1u} is responsible for both Na and Nb displacements which are investigated separately.

the T_{1u} and E_{u2}. Figure 9 represents the APESCSs for these submodes, based on which the Nb displacement with the T_{1u} irrep is the distortion creating the instability in the cubic phase at Γ, while along whether the T_{1u} mode for Na, or E_{u2} mode, no destabilization of the ground or stabilization of the excited state exists. This yields that the Nb displacement induced by the coupling of the (T_{2u}, T_{2g}) states and the (T_{2u}, E_g) states is the distortion responsible for cubic structure instability at Γ. Based on the energy gaps between the (T_{2u}, T_{2g}) states and between the (T_{2u}, E_g) states, and the K_V term in Eq. (2), the overlap is mostly between the O-$2p$ and Nb-$4d$–T_{2g} orbitals compared to the O-$2p$ and Nb-$4d$–E_g orbitals. Compared to the PbZrO$_3$ case, the Σ_2 mode, recognized as the original mode [26], contains both Pb and Zr AFE instabilities, while the S_4 mode contains only the Pb AFE displacements, agreeing with the primary role of the B-site cation instability in our conclusion.

2. Cubic-FE phase transition

In the cubic-FE phase transition, the irrep of the R_5^- and M_2^+ modes is E_u, and the Γ_4^- mode consists of three irreps, as $T_{1u} + A_{2u} + E_u$. Based on symmetry analysis in Eqs. (3)–(7) the couplings of the (T_{2u}, T_{2g}) and (T_{1u}, T_{2g}) electronic states could be done by Γ_4^-, M_2^+, and R_5^- modes, while the (T_{2u}, E_g), (T_{1u}, A_{1g}), and (T_{1u}, E_g) electronic state couplings are possible only by the Γ_4^- mode. As the sufficient condition, the APESCSs at Γ are studied based on Fig. 10. The results show that based on PJTE, the driving force for the phase transition at Γ is primarily done by the Γ_4^- mode. The mode is induced by the couplings of the (T_{2u}, T_{2g}) states and (T_{2u}, E_g) states, and by the (T_{1u}, T_{2g}) states and (T_{1u}, E_g) states at Γ. Due to the smaller

band gap, the couplings are more strong when the excited state T_{2g} contributes, compared to that in which the E_g state plays the role as the excited state. The APESCSs related to the R_5^- and M_2^+ modes show no manifestation of the strong PJTE and are not considered as the modes destabilizing the cubic phase at Γ. Therefore, in the cubic-FE phase transition, the electronic driving force at Γ is achieved by both T_{2u} and T_{1u} states participating as the ground state, whereas, interestingly, as seen in Fig. 8, in the case of the cubic-AFE phase transition, that is due to the couplings in which only the T_{2u} state plays the role as the ground state.

IV. CONCLUSIONS

In this study, based on the potential energy surface and the invariant polynomial for the primary modes, it can be concluded that the coupling of the three primary modes, studied by the trilinear term in the Hamiltonian polynomial, plays an essential role in the stabilization of the AFE phase. Besides, the AFE-AFD modes coexistence, in both the presence and absence of strain modes, is in favor of the AFE phase stabilization, while for the coexistence of the AFD modes, either the strain modes or the AFE mode, or both, are required to decrease the energy.

Moreover, based on the symmetry analysis and APESCSs, following the theory of PJTE with the focus on the second order terms of the APES expansion, it is observed that the primary mode originating the destabilization of the cubic phase at Γ in the PE-AFE phase transition is the AFE mode. That, in the case of the PE-FE phase transition, is identified to be the FE mode. Interestingly, in both cases, the AFD modes do
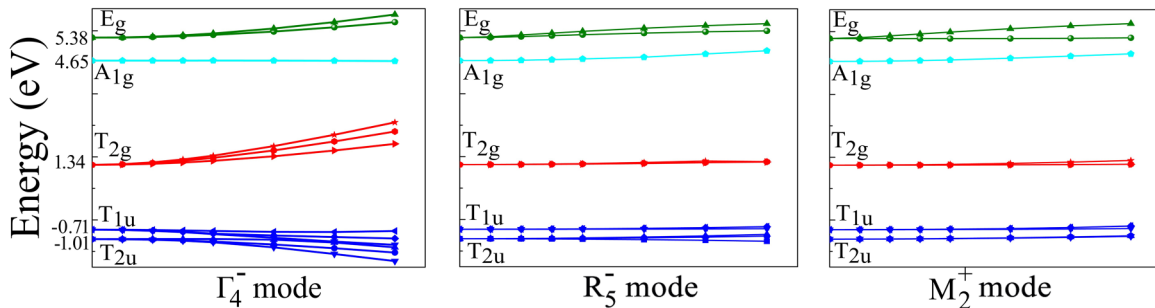

FIG. 10. APESCSs at Γ along the Γ_4^-, R_5^-, and M_2^+ modes. Γ_4^- is the primary mode, induced mostly by the couplings of the (T_{2u}, T_{2g}) and (T_{1u}, T_{2g}) states.

not participate in the strong PJTE at the Γ point; however, they can be the reason of instability in the other points of the BZ.

The electronic structure origin of the PE-AFE phase transition at Γ is concluded to be the coupling of (T_{2u}, T_{2g}) electronic states by PJTE, inducing the AFE Δ_5 mode, while both the (T_{1u}, T_{2g}) state and (T_{2u}, T_{2g}) state couplings via the FE Γ_4^- mode are the electronic driving force behind the cubic to FE phase transition at Γ. In other words, in the PE-FE phase transition, both states of the O-2p orbital contribute to the couplings, while, in the PE-AFE case, only the T_{2u} state participates in coupling to originate the phase transition.

Such conclusions can shed more light on the identification of the electronic structure descriptors for the NaNbO$_3$-based and other AFE/FE materials, and pave the way to design the new (hopefully lead-free) AFE/FE materials. Moreover, success of the PJTE raises it as a valuable approach in figuring out the driving forces of the FE/AFE materials to guide the engineering of novel functionalities and materials for optimal properties.

[1] R. E. Jones, Ferroelectric nonvolatile memories for embedded applications, in *Proceedings of the IEEE 1998 Custom Integrated Circuits Conference, Santa Clara, CA, USA* (IEEE, New York, 1998), pp. 431–438.

[2] J. F. Scott and C. A. Paz de Araujo, Ferroelectric memories, Science **246**, 1400 (1989).

[3] M. M. Vopson, G. Caruntu, and X. Tan, Polarization reversal and memory effect in anti-ferroelectric materials, Scr. Mater. **128**, 61 (2017).

[4] G. R. Love, Energy storage in ceramic dielectrics, J. Am. Ceram. Soc. **73**, 323 (1990).

[5] Z. Liu, T. Lu, J. Ye, G. Wang, X. Dong, R. Withers, and Y. Liu, Antiferroelectrics for energy storage applications: A review, Adv. Mater. Technol. **3**, 1800111 (2018).

[6] X. Hao, A review on the dielectric materials for high energy-storage application, J. Adv. Dielect. **3**, 1330001 (2013).

[7] A. Devonshire, Theory of ferroelectrics, Adv. Phys. **3**, 85 (1954).

[8] W. Cochran, Crystal stability and the theory of ferroelectricity, Phys. Rev. Lett. **3**, 412 (1959).

[9] M. E. Lines and A. M. Glass, *Principles and Applications of Ferroelectrics and Related Materials* (Oxford University Press, Oxford, 2001).

[10] V. Polinger, P. Garcia-Fernandez, and I. Bersuker, Pseudo Jahn-Teller origin of ferroelectric instability in BaTiO$_3$ type perovskites: The Green's function approach and beyond, Phys. B: Condens. Matter **457**, 296 (2015).

[11] R. E. Cohen, Origin of ferroelectricity in perovskite oxides, Nature (London) **358**, 136 (1992).

[12] D. J. Singh, Structure and energetics of antiferroelectric PbZrO$_3$, Phys. Rev. B **52**, 12559 (1995).

[13] I. Bersuker, On the origin of ferroelectricity in perovskite-type crystals, Phys. Lett. **20**, 589 (1966).

[14] K. Tkacz-Śmiech, A. Koleżyński, and W. Ptak, Chemical bond in ferroelectric perovskites, Ferroelectrics **237**, 57 (2000).

[15] A. F. Devonshire, XCVI. Theory of barium titanate: Part I, Lond. Edinb. Dublin philos. mag. j. sci. **40**, 1040 (1949).

[16] I. B. Bersuker, Pseudo-Jahn–Teller effect: A two-state paradigm in formation, deformation, and transformation of molecular systems and solids, Chem. Rev. **113**, 1351 (2013).

[17] I. B. Bersuker and V. Z. Polinger, *Vibronic Interactions in Molecules and Crystals* (Springer Science & Business Media, New York, 2012).

[18] C. Kittel, Theory of antiferroelectric crystals, Phys. Rev. **82**, 729 (1951).

[19] E. Sawaguchi, H. Maniwa, and S. Hoshino, Antiferroelectric structure of lead zirconate, Phys. Rev. **83**, 1078 (1951).

[20] Z. Zhou, Q. Yang, M. Liu, Z. Zhang, X. Zhang, D. Sun, T. Nan, N. Sun, and X. Chen, Antiferroelectric materials, applications and recent progress on multiferroic heterostructures, SPIN **5**, 1530001 (2015).

[21] H. D. Megaw, The seven phases of sodium niobate, Ferroelectrics **7**, 87 (1974).

[22] A. Hewat, Neutron powder profile refinement of ferroelectric and antiferroelectric crystal structures: Sodium niobate at 22 °C, Ferroelectrics **7**, 83 (1974).

[23] G. Shirane, E. Sawaguchi, and Y. Takagi, Dielectric properties of lead zirconate, Phys. Rev. **84**, 476 (1951).

[24] G. Shirane, Ferroelectricity and antiferroelectricity in ceramic PbZrO$_3$ containing Ba or Sr, Phys. Rev. **86**, 219 (1952).

[25] D. Vanderbilt and W. Zhong, First-principles theory of structural phase transitions for perovskites: Competing instabilities, Ferroelectrics **206**, 181 (1998).

[26] A. Tagantsev, K. Vaideeswaran, S. Vakhrushev, A. Filimonov, R. Burkovsky, A. Shaganov, D. Andronikova, A. Rudskoy, A. Baron, H. Uchiyama *et al.*, The origin of antiferroelectricity in PbZrO$_3$, Nat. Commun. **4**, 2229 (2013).

[27] J. Íñiguez, M. Stengel, S. Prosandeev, and L. Bellaiche, First-principles study of the multimode antiferroelectric transition in PbZrO$_3$, Phys. Rev. B **90**, 220103(R) (2014).

[28] S. Gabuda, S. Kozlova, and N. Dalal, Vibronic model for antiferroelectric phase transition in squaric acid, H$_2$C$_4$O$_4$, Solid State Commun. **130**, 729 (2004).

[29] A. Audzijonis, R. Sereika, L. Žigas, and R. Žaltauskas, Dielectric and electrical properties of SbSi and SbSeI single crystals in

the region of antiferroelectric phase transition, J. Phys. Chem. Solids **83**, 117 (2015).

[30] B. Matthias, New ferroelectric crystals, Phys. Rev. **75**, 1771 (1949).

[31] L. E. Cross and B. J. Nicholson, LV. The optical and electrical properties of single crystals of sodium niobate, Lond. Edinb. Dublin Philos. Mag. J. Sci. **46**, 453 (1955).

[32] J. Chen and D. Feng, TEM study of phases and domains in NaNbO$_3$ at room temperature, Phys. Status Solidi A **109**, 171 (1988).

[33] R. A. Shakhovoy, S. I. Raevskaya, L. A. Shakhovaya, D. V. Suzdalev, I. P. Raevski, Y. I. Yuzyuk, A. F. Semenchev, and M. El Marssi, Ferroelectric *Q* and antiferroelectric *P* phases' coexistence and local phase transitions in oxygen-deficient NaNbO$_3$ single crystal: Micro-Raman, dielectric and dilatometric studies, J. Raman Spectrosc. **43**, 1141 (2012).

[34] M.-H. Zhang, L. Fulanović, S. Egert, H. Ding, P. B. Groszewicz, H.-J. Kleebe, L. Molina-Luna, and J. Koruza, Electric-field-induced antiferroelectric to ferroelectric phase transition in polycrystalline NaNbO$_3$, Acta Mater. **200**, 127 (2020).

[35] S. K. Mishra, N. Choudhury, S. L. Chaplot, P. S. R. Krishna, and R. Mittal, Competing antiferroelectric and ferroelectric interactions in NaNbO$_3$: Neutron diffraction and theoretical studies, Phys. Rev. B **76**, 024110 (2007).

[36] A. M. Glazer and H. D. Megaw, The structure of sodium niobate (T$_2$) at 600 °C, and the cubic-tetragonal transition in relation to soft-phonon modes, Philos. Mag. **25**, 1119 (1972).

[37] M. Ahtee, A. M. Glazer, and H. D. Megaw, The structures of sodium niobate between 480° and 575 °C, and their relevance to soft-phonon modes, Philos. Mag. **26**, 995 (1972).

[38] A. C. Sakowski-Cowley, K. Łukaszewicz, and H. D. Megaw, The structure of sodium niobate at room temperature, and the problem of reliability in pseudosymmetric structures, Acta Cryst. B **25**, 851 (1969).

[39] C. N. W. Darlington and H. D. Megaw, The low-temperature phase transition of sodium niobate and the structure of the low-temperature phase, *N*, Acta Cryst. B **29**, 2171 (1973).

[40] S. G. Jabarov, D. P. Kozlenko, S. E. Kichanov, A. V. Belushkin, A. I. Mammadov, B. N. Savenko, R. Z. Mekhtieva, and C. Lathe, Structural studies of the P-T phase diagram of sodium niobate, J. Surf. Invest. **6**, 546 (2012).

[41] S. K. Mishra, R. Mittal, V. Y. Pomjakushin, and S. L. Chaplot, Phase stability and structural temperature dependence in sodium niobate: A high-resolution powder neutron diffraction study, Phys. Rev. B **83**, 134105 (2011).

[42] R. D. Shannon and C. T. Prewitt, Effective ionic radii in oxides and fluorides, Acta Cryst. B **25**, 925 (1969).

[43] D. S. Gyan, A. A. Goyal, Y. Tamrakar, and A. Dwivedi, Stabilization of anti-ferroelectric *Pbcm* phase over ferroelectric *P*2$_1$*ma* phase in intermittent ferroelectric NaNbO$_3$ by incorporating CaTiO$_3$, J. Phys. D **52**, 165304 (2019).

[44] R. Dungan and R. Golding, Metastable ferroelectric sodium niobate, J. Am. Ceram. Soc. **47**, 73 (1964).

[45] T. Arioka, H. Taniguchi, M. Itoh, K. Oka, R. Wang, and D. Fu, Ferroelectricity in NaNbO$_3$: Revisited, Ferroelectrics **401**, 51 (2010).

[46] M. Zhang, N. Hadaeghi, S. Egert, H. Ding, H. Zhang, P. Groszewicz, G. Buntkowsky, A. Klein, and J. Koruza, Design of lead-free antiferroelectric (1 − *x*)NaNbO$_3$-*x*SrSnO$_3$ compo-

sitions guided by first-principles calculations, Chem. Mater. **33**, 266 (2021).

[47] H. Shimizu, H. Guo, S. E. Reyes-Lillo, Y. Mizuno, K. M. Rabe, and C. A. Randall, Lead-free antiferroelectric: *x*CaZrO$_3$-(1 − *x*)NaNbO$_3$ system (0 ⩽ *x* ⩽ 0.10), Dalton Trans. **44**, 10763 (2015).

[48] K. E. Johnston, C. C. Tang, J. E. Parker, K. S. Knight, P. Lightfoot, and S. E. Ashbrook, The polar phase of NaNbO$_3$: A combined study by powder diffraction, solid-state NMR, and first-principles calculations, J. Am. Chem. Soc. **132**, 8732 (2010).

[49] D. Yang, Y. Zhang, X. Wang, Q. Li, and J.-F. Li, Antiferroelectricity of NaNbO$_3$: Single-crystal experimental study and first-principles calculation, J. Am. Ceram. Soc. **105**, 5555 (2022).

[50] I. B. Bersuker, N. N. Gorinchoi, and T. A. Fedorco, Band structure and vibronic coupling related to ferroelectric properties of titanates of Ca, Sr and Ba, Ferroelectrics **153**, 1 (1994).

[51] K. Momma and F. Izumi, VESTA: A three-dimensional visualization system for electronic and structural analysis, J. Appl. Cryst. **41**, 653 (2008).

[52] G. Kresse and D. Joubert, From ultrasoft pseudopotentials to the projector augmented-wave method, Phys. Rev. B **59**, 1758 (1999).

[53] G. Kresse and J. Hafner, *Ab initio* simulation of the metal/nonmetal transition in expanded fluid mercury, Phys. Rev. B **55**, 7539 (1997).

[54] G. Kresse and J. Furthmüller, Efficient iterative schemes for *ab initio* total-energy calculations using a plane-wave basis set, Phys. Rev. B **54**, 11169 (1996).

[55] S. P. Solov'ev, Y. N. Venevtsev, and G. S. Zhanov, An x-ray study of phase transitions in NaNbO$_3$, Kristallografiya **6**, 218 (1961) [Sov. Phys. Cryst. **6**, 171 (1961)].

[56] E. Sjöstedt, L. Nordström, and D. Singh, An alternative way of linearizing the augmented plane-wave method, Solid State Commun. **114**, 15 (2000).

[57] G. K. H. Madsen, P. Blaha, K. Schwarz, E. Sjöstedt, and L. Nordström, Efficient linearization of the augmented plane-wave method, Phys. Rev. B **64**, 195134 (2001).

[58] P. Blaha, K. Schwarz, P. Sorantin, and S. B. Trickey, Full-potential, linearized augmented plane wave programs for crystalline systems, Comput. Phys. Commun. **59**, 399 (1990).

[59] K. Koepernik and H. Eschrig, Full-potential nonorthogonal local-orbital minimum-basis band-structure scheme, Phys. Rev. B **59**, 1743 (1999).

[60] I. Opahle, K. Koepernik, and H. Eschrig, Full-potential band-structure calculation of iron pyrite, Phys. Rev. B **60**, 14035 (1999).

[61] J. P. Perdew, K. Burke, and M. Ernzerhof, Generalized gradient approximation made simple, Phys. Rev. Lett. **77**, 3865 (1996).

[62] H. J. Monkhorst and J. D. Pack, Special points for Brillouin-zone integrations, Phys. Rev. B **13**, 5188 (1976).

[63] H. Stokes, D. Hatch, and B. Campbell, ISOTROPY software suite, https://iso.byu.edu/iso/isotropy.php.

[64] H. T. Stokes and D. M. Hatch, *Isotropy Subgroups of the 230 Crystallographic Space Groups* (World Scientific, Singapore, 1988).

[65] G. Y. Lyubarskii, *The Application of Group Theory in Physics* (Elsevier, Amsterdam, 2013).

[66] D. M. Hatch and H. T. Stokes, INVARIANTS: Program for obtaining a list of invariant polynomials of the order-parameter components associated with irreducible representations of a space group, J. Appl. Cryst. **36**, 951 (2003).

[67] W. Zhong and D. Vanderbilt, Competing structural instabilities in cubic perovskites, Phys. Rev. Lett. **74**, 2587 (1995).

[68] B. K. Mani, S. Lisenkov, and I. Ponomareva, Finite-temperature properties of antiferroelectric $PbZrO_3$ from atomistic simulations, Phys. Rev. B **91**, 134112 (2015).

[69] Y. Xie, H.-G. Fu, H.-T. Yu, G.-X. Zhang, and J.-Z. Sun, A first-principles investigation into the ferroelectric and antiferrodistortive instabilities of cubic $SrTiO_3$, J. Phys.: Condens. Matter **19**, 506213 (2007).

[70] K. M. Rabe and P. Ghosez, First-principles studies of ferroelectric oxides, in *Physics of Ferroelectrics* (Springer, Berlin, 2007), pp. 117–174.

[71] T. Gu, T. Scarbrough, Y. Yang, J. Iniguez, L. Bellaiche, and H. J. Xiang, Cooperative couplings between octahedral rotations and ferroelectricity in perovskites and related materials, Phys. Rev. Lett. **120**, 197602 (2018).

[72] See Supplemental Material at http://link.aps.org/supplemental/10.1103/PhysRevMaterials.8.015004 for additional information regarding the AFE-FE phase transition and the cubic-FE potential energy curve.

[73] I. Bersuker, *The Jahn-Teller Effect* (Cambridge University Press, Cambridge, 2006).

[74] U. Öpik and M. H. L. Pryce, Studies of the Jahn-Teller effect. I. A survey of the static problem, Proc. R. Soc. London A **238**, 425 (1957).

[75] I. B. Bersuker, N. N. Gorinchoi, and V. Z. Polinger, On the origin of dynamic instability of molecular systems, Theor. Chim. Acta **66**, 161 (1984).

[76] I. B. Bersuker, Are activated complexes of chemical reactions experimentally observable ones, Nouv. J. Chim. **4**, 139 (1980).

[77] R. Bader, An interpretation of potential interaction constants in terms of low-lying excited states, Mol. Phys. **3**, 137 (1960).

[78] R. F. Bader, Vibrationally induced perturbations in molecular electron distributions, Can. J. Chem. **40**, 1164 (1962).

[79] R. Bader and A. Bandrauk, Relaxation of the molecular charge distribution and the vibrational force constant, J. Chem. Phys. **49**, 1666 (1968).

[80] R. G. Pearson, *Symmetry Rules for Chemical Reactions* (Wiley, 1976).

[81] R. C. Powell, *Symmetry, Group Theory, and the Physical Properties of Crystals* (Springer, Berlin, 2010).

[82] C. Linderälv, A. Lindman, and P. Erhart, A unifying perspective on oxygen vacancies in wide band gap oxides, J. Phys. Chem. Lett. **9**, 222 (2018).

[83] C. Shen, N. Hadaeghi, H. K. Singh, T. Long, L. Fan, G. Qin, and H. Zhang, Two-dimensional buckling structure induces the ultra-low thermal conductivity: A comparative study of the group GaX (X = N, P, As), J. Mater. Chem. C **10**, 1436 (2022).

[84] Y. Liu, I. B. Bersuker, P. Garcia-Fernandez, and J. E. Boggs, Pseudo Jahn-Teller origin of nonplanarity and rectangular-ring structure of tetrafluorocyclobutadiene, J. Phys. Chem. A **116**, 7564 (2012).

[85] J. Chen and D. Feng, In situ TEM studies of para-ferro phase transitions in $NaNbO_3$, Phys. Status Solidi A **109**, 427 (1988).

[86] X. Wang, Z. Shen, Z. Hu, L. Qin, S. Tang, and M. Kuok, High temperature Raman study of phase transitions in antiferroelectric $NaNbO_3$, J. Mol. Struct. **385**, 1 (1996).

[87] D. Viehland, Transmission electron microscopy study of high-Zr-content lead zirconate titanate, Phys. Rev. B **52**, 778 (1995).